

19

20 **Abstract**

21 Prediction skills of summer precipitations over southern Africa (16° - 33° E, 22° - 35° S) in
22 the SINTEX-F coupled model are assessed for the period of 1982-2008. Using three different
23 observation datasets, deterministic forecasts are evaluated by anomaly correlation coefficients,
24 whereas scores of relative operating characteristic and relative operating level are used to
25 evaluate probabilistic forecasts. It is shown that these scores for forecasts of
26 December-February precipitation initialized on October 1st are significant at 95% confidence
27 level. On a local scale, the prediction skills in the northwestern and central parts of southern
28 Africa are higher than those in northeastern South Africa. El Niño/Southern Oscillation
29 (ENSO) provides the major source of predictability, but the relationship with ENSO is
30 over-confident in the model. Also, the Benguela Niño, the basin mode in the tropical Indian
31 Ocean, the subtropical dipole modes in the South Atlantic and the southern Indian Oceans and
32 ENSO Modoki may provide additional sources of predictability. When prediction skills are
33 evaluated for the whole wet season from October to the following April, it is found that
34 precipitation anomalies in December-February are most predictable. The present study
35 presents promising results for seasonal prediction of precipitation anomalies in the
36 extratropics, where seasonal forecast are considered a difficult task.

37

38

39

40 **1. Introduction**

41 Precipitation over most of southern Africa shows a distinct seasonality with a wet
42 season in austral summer and a dry season in austral winter. It undergoes significant
43 interannual variations with El Niño/Southern Oscillation (ENSO) playing a key role (Dyer
44 1979; Lindesay 1988; Reason et al. 2000; Reason and Rouault 2002; Rouault and Richard
45 2005). In La Niña years, cloud bands related to the South Indian Convergence Zone tend to be
46 preferentially located over southern Africa, resulting in higher precipitation. On the other
47 hand, the cloud bands tend to move northeastward to Madagascar in El Niño years, leading to
48 dry conditions in southern Africa (e.g., Cook 2000; Hart et al. 2010, 2012). However, the
49 ENSO influences are neither simple nor exclusive. For example, the 1997/1998 El Niño, the
50 strongest event on record, was not accompanied by the driest summer in subtropical southern
51 Africa (Lyon and Mason 2007). Also, their link undergoes large decadal variations (Richard
52 et al. 2000), and can be modified by local systems such as Angola low (Reason and
53 Jagadheesha 2005; Lyon and Mason 2007).

54 Besides ENSO, large-scale atmospheric circulation anomalies associated with the
55 subtropical dipole modes in the South Atlantic and the southern Indian Ocean (e.g., Venegas
56 et al. 1997; Behera and Yamagata 2001) may modulate precipitation through their impacts on
57 moisture transport (Behera and Yamagata 2001; Reason 2001, 2002; Vigaud et al. 2009).
58 Also, recent studies showed that the subtropical dipole modes are closely related to the
59 synoptic rain-bearing systems passing through southern Africa such as the tropical temperate
60 troughs (Harrison 1984; Todd and Washington 1999; Fauchereau et al. 2009; Pohl et al. 2009;

61 Ratna et al. 2012; Vigaud et al. 2012). Furthermore, tropical cyclones (Reason and Keibel
62 2004), Angola low (Lyon and Mason 2007), Benguela upwelling system (Walker 1990) and
63 Agulhas Current (Mason 1995; Tyson and Preston-Whyte 2004) exert influences on the
64 southern African summer precipitation. Complex interactions among them make the seasonal
65 prediction a difficult task.

66 Agriculture in southern Africa is predominantly rain-fed and thus highly vulnerable to
67 rainfall variations, but measures to mitigate impacts of the interannual variations are still far
68 below satisfaction (Conway 2009). To increase resilience of local communities and
69 households, it is crucial to understand causes of rainfall variations, to make an accurate
70 prediction, and to implement an early warning system and countermeasures. For this reason,
71 the South African modeling community has developed operational seasonal forecasting
72 systems (e.g., Barnston et al. 1996; Mason et al 1996; Landman and Mason 1999; Landman et
73 al. 2001). The earlier systems relied on statistical methods and often adopted sea surface
74 temperature (SST) in the adjacent subtropical oceans and/or the remote tropical eastern
75 Pacific as predictors. More recently, they were replaced by two- and one-tiered dynamical
76 forecast systems, but raw model outputs, such as geopotential height at 850 hPa, are often
77 statistically downscaled to achieve better prediction skills of the southern African summer
78 precipitation (e.g., Landman and Goddard 2002; Landman et al. 2012; Landman and Beraki
79 2012). This is because general circulation models tend to simulate large-scale circulation
80 anomalies more accurately than precipitation anomalies (Landman and Goddard 2002). One
81 of the reasons is that typical resolution of general circulation models (100-200 km) is too
82 coarse to adequately resolve complex topography that is important to the local precipitation.

83 For this reason, some recent studies have developed dynamical downscaling systems for
84 southern Africa using high-resolution regional models (Ratnam et al. 2011; Boulard et al.
85 2012; Crétat et al. 2012), but these models require good side boundary conditions provided by
86 a global model.

87 In this regard, CGCMs have made big progresses in seasonal forecasts not only for the
88 tropical climate variations (e.g., Luo et al. 2007; Jin et al. 2008; Barnston et al. 2012), but also
89 for extratropical climate variations. Yuan et al. (2013) showed for the first time that the SST
90 anomalies even in the subtropical oceans are predictable at around one season lead when they
91 assessed predictability of the subtropical dipole modes. This presents a great potential for the
92 CGCMs to predict the seasonal climate variations in the mid-latitudes, and encourages further
93 development of CGCMs for mid-latitudes applications.

94 In this study, using the same CGCM as in Yuan et al. (2013), seasonal forecasts of the
95 summer precipitation in southern Africa (16° - 33° E and 22° - 35° S, shown by the white box in
96 Fig. 1a) are evaluated for the period of 1982-2008. A special emphasis is placed on
97 precipitation anomalies in December-February (DJF), corresponding to the peak of the wet
98 season in southern Africa. The model forecasts of the precipitation in DJF are verified against
99 observations without any post-processing, and thus successful forecasts may be related to
100 realistic reproductions of large-scale circulation anomalies responsible for observed
101 precipitation anomalies. Therefore, by comparing the predicted and observed SST and
102 large-scale circulation anomalies, possible sources of predictability may be investigated as
103 well.

104 This paper is organized as follows. A brief description of the CGCM, retrospective

105 forecast experiments, and verification data and methods is given in the next section. In
106 Section 3, the prediction skills for the precipitation anomalies in DJF when the model is
107 initialized on October 1st are assessed. Possible sources of predictability are discussed in
108 Section 4. Section 5 examines how prediction skills vary during the wet season. The final
109 section is reserved for conclusions.

110

111 **2. Model, retrospective forecasts, and verification data and methods**

112 **2.1. Model and retrospective forecasts**

113 The Scale Interaction Experiment-Frontier Research Center for Global Change CGCM
114 (SINTEX-F, see Luo et al. 2003 and 2005a for details) is used in this study. The oceanic
115 component is the reference version 8.2 of Océan Parallélisé (Madec et al. 1998). It has 31
116 vertical levels and horizontal resolution of 2° with increased meridional resolution of 0.5° near
117 the equator. The atmospheric component is the latest version of ECHAM4 (Roeckner et al.
118 1996) with 19 vertical levels and a horizontal resolution of T106. The coupled model has been
119 used to successfully simulate and predict the tropical climate modes such as ENSO and the
120 Indian Ocean Dipole and their teleconnections to the mid-high latitudes (e.g., Yamagata et al.
121 2004; Tozuka et al. 2005; Luo et al. 2005b, 2007, 2008). It has higher skills in simulating the
122 Indian Ocean subtropical dipole mode than the Coupled Model Inter-comparison Project
123 phase-3 (CMIP3) coupled models (Kataoka et al. 2012), and can skillfully predict the Indian
124 Ocean and South Atlantic subtropical dipole modes with about one season lead (Yuan et al.
125 2013). In this study, a series of nine-member ensemble forecasts is conducted by the coupled
126 model. The forecasts are initialized on the first day of each month from February 1982 to

127 December 2008 and integrated for 12 months. The nine ensemble members differ in initial
128 conditions and/or coupling physics. Readers are referred to Luo et al. (2007) and Yuan et al.
129 (2013) for more details.

130

131 **2.2. Verification data and methods**

132 The precipitation forecasts are verified against three different observations: Global
133 Precipitation Climatology Project monthly precipitation (GPCP; 2.5°x2.5°; Adler et al. 2003),
134 Global Precipitation Climatology Centre monthly precipitation (GPCC; 2.5°x2.5°; land only;
135 Schneider et al. 2013) and Africa Rainfall Climatology version 2 daily precipitation estimates
136 (ARC2; 0.1°x0.1°; Love et al. 2004). Although there are some missing data, an average of
137 available dates in a month/season is used to calculate the monthly/seasonal mean of ARC2.
138 The predicted SSTs and atmospheric fields are verified against the monthly Optimum
139 Interpolation SST (OISST; 1°x1°; Reynolds et al. 2002) and three different reanalysis datasets,
140 respectively. The latter includes the National Centers for Environmental Prediction/National
141 Center for Atmospheric Research reanalysis 1 (NCEP/NCAR; 2.5°x2.5°; Kalnay et al. 1996),
142 the European Centre for Medium-Range Weather Forecasts Interim Reanalysis (ERA-Interim;
143 1.5°x1.5°; Dee et al. 2011) and the NCEP climate forecast system reanalysis (CFSR;
144 2.5°x2.5°; Saha et al. 2010). We note that the data above have various horizontal resolutions
145 and are interpolated to the model grids when needed.

146 Figure 1 shows the climatology of precipitation and moisture fluxes at 850 hPa in DJF.
147 All three precipitation datasets show east-west gradient with the maximum in eastern South
148 Africa separated from the inter-tropical convergence zone to the north. However, the

149 maximum precipitation is slightly larger in the GPCP than in the GPCC and ARC2 (Figs.
150 1a-c). The moisture fluxes to the southern African subcontinent are mainly from the Indian
151 Ocean, and they are slightly stronger in the ERA-Interim than in the NCEP/NCAR and CFSR.
152 Nevertheless, there are no significant differences in the three observed precipitation and
153 reanalysis data. The model successfully simulates the observed precipitation pattern (Fig. 1d),
154 but the simulated amount is about twice as large as the observed, because the simulated
155 moisture fluxes to the subcontinent in the lower troposphere are much stronger and extend
156 farther to the west compared to the reanalysis data. Similar wet biases have been reported in
157 many general circulation and regional models (e.g., Joubert 1997; Ratnam et al. 2011; Crétat
158 et al. 2012). To exclude the model biases in the climatology, predicted anomalies are verified
159 against the observations after removing the monthly climatology in each dataset (Kirtman et
160 al. 1997).

161 The southern African precipitation index in this study is defined as precipitation
162 anomalies averaged over the southern African region of interest (16° - 33° E, 22° - 35° S; see the
163 white box in Fig. 1a). Deterministic forecasts are evaluated by anomaly correlation coefficient
164 (ACC; Pearson's correlation coefficient) between the ensemble-mean forecasts and
165 observations. Its statistical significance is tested by the one-tailed *t*-test since the predicted
166 and observed precipitation anomalies are supposed to correlate positively. Probabilistic
167 forecasts for the above- and below-normal precipitation are evaluated by scores of the relative
168 operating characteristic (ROC) and relative operating level (ROL) (Mason and Graham 1999).
169 The threshold value for above (below)-normal tercile is the lowest (highest) value in the
170 highest (lowest) 33% of the historical records. The ROC and ROL scores are equivalent to the

171 areas beneath the ROC and ROL curves. The ROC curve reflects the ratios between the hit
172 rate and the false-alarm rate when the forecast probability to issue an above/below-normal
173 precipitation year is decreased gradually. Here, the hit (false-alarm) rate is the proportion of
174 years in the above/below-normal tercile (other terciles) that are correctly (incorrectly)
175 predicted as the above/below-normal precipitation year. The ROL curve reflects the ratios
176 between the correct-alarm ratio and the miss ratio when the number of years in the
177 above/below-normal tercile is increased gradually, and the forecast for above/below-normal
178 precipitation are issued when at least 33% of the ensemble members are in
179 above/below-normal tercile. Here, the correct-alarm (miss) ratio is defined as the probability
180 that an above/below-normal year will occur when it is forecasted (not forecasted). If the ROC
181 and ROL scores are better than 0.5, the forecast system is regarded to have skills in
182 discriminating the above/below-normal precipitation, and the higher the scores, the better the
183 skills are. The statistical significance of the scores is tested by the Mann-Whitney U-test
184 (Manson and Graham 2002). We note that all ROC and ROL scores shown in this study are
185 cross-validated by a leave-one-out manner, such that the threshold is computed using all years
186 except for the year being considered.

187 Since the ROC and ROL scores cannot reflect the reliability of the forecast probabilities,
188 the reliability diagram is also provided (Wilks 1995). In the reliability diagram, the forecast
189 probabilities are plotted against frequency by which the forecasts are verified (i.e. the
190 observed relative frequency). Ideally, the reliability curve is along the 45° diagonal line,
191 which signifies the identical forecast probability and observed relative frequency. If the curve
192 lies above (below) the 45° diagonal line, the forecast system is under (over)-confident.

193 Besides being reliable, the forecast probabilities are desired to span away from the
194 climatological probability, which is 33% in this study. The reason is that even without model
195 predictions, the probability for the precipitations in each year to fall in the
196 above/below-normal tercile is 33%.

197

198 **3. Prediction skills for the DJF southern African precipitations**

199 **3.1. Deterministic forecasts**

200 Figure 2 shows the time series of the southern African precipitation indices in DJF
201 obtained from the model forecasts initialized on October 1st and the GPCP. Since the index
202 based on GPCC (ARC2) is similar to that based on the GPCP with correlation coefficients of
203 0.99 (0.84), it is not shown in Fig. 2. The ensemble-mean forecasts have high correlations
204 with the observation; when verified against the GPCP, GPCC and ARC2, the ACCs are 0.68,
205 0.66 and 0.61, respectively. These are significant at 99.95% confidence level by the one-tailed
206 *t*-test and higher than 0.6, the threshold value of high prediction skills for seasonal
207 precipitation (Marengo et al. 2005). We note that the observed precipitation index falls within
208 the model's interquartile range in only seven out of 27 years, because the standard deviation
209 of precipitation anomalies in each ensemble member is only two-third of the observation.
210 Also, the large ensemble spread is due to one or two outliers.

211 The Spearman's (Kendall's tau rank) correlation coefficients are 0.71, 0.70 and 0.63
212 (0.55, 0.52 and 0.45), when the 27-year deterministic forecasts shown in Fig. 2 are verified
213 against the GPCP, GPCC, and ARC2, respectively. All of these correlation coefficients are
214 significant at 99.95% confidence level, and higher than those obtained in past studies. For

215 instance, using prediction results of three CGCMs from the Development of a European
216 Multimodel Ensemble System for Seasonal-to-Interannual Prediction Project (DEMETER)
217 initialized on November 1st, Landman and Beraki (2012) obtained statistically downscaled
218 forecasts for DJF southern African precipitations averaged south of 10°S. When their
219 deterministic forecasts were verified against the University of East Anglia Climatic Research
220 Unit (CRU; Mitchell and Jones 2005) monthly precipitation data for the 21-year test period
221 from 1980/1981 to 2001/2002, the Spearman's rank correlation coefficient was slightly less
222 than 0.5, significant at 95% confidence level. Also, for the 14-year test period from
223 1995/1996 to 2008/2009, the Kendall's tau rank correlation coefficient between the predicted
224 rainfall in DJF obtained from statistical downscaling of a coupled model
225 (ECHAM4.5-MOM3-DC2; DeWitt 2005) prediction initialized at the end of October and the
226 rainfall data from the South African Weather Service (Van Rooy 1972) was 0.45, significant
227 at 95% confidence level (Landman et al. 2012). Although there exist some differences in
228 precipitation data used to evaluate the model, data period, area used to calculate average
229 precipitation, and lead-time of seasonal forecasts, the high correlation coefficients obtained in
230 this study suggest that the SINTEX-F has high skills in predicting the southern African
231 summer precipitation.

232 Figure 3 shows the ACCs of predicted precipitation anomalies with the three different
233 observations at each model grid in the southern African region of interest. Although the ACCs
234 are somewhat higher with GPCP, their spatial distributions are quite similar; the ACCs
235 significant at 95% confidence level are mostly confined to the northwestern and central part
236 of southern Africa, while very low ACCs are found in northeastern South Africa. This is

237 contrasted to many other models showing the highest prediction skills in northeastern South
238 Africa (e.g., Landman et al. 2012). Hence, a multi-model ensemble forecast system for the
239 southern African summer precipitation may benefit from inclusion of the SINTEX-F, as it
240 provides distinct and independent prediction skills (Hagedorn et al. 2005).

241

242 **3.2. Probabilistic forecasts**

243 The leave-one-out cross-validated ROC scores for the above (below)-normal DJF
244 southern African precipitation indices in DJF are 0.76, 0.76 and 0.80 (0.79, 0.82 and 0.78),
245 respectively, when the probabilistic forecasts are verified against the GPCP, GPCC and ARC2
246 (Fig. 4a). The corresponding ROL scores are 0.84, 0.84 and 0.80 (0.85, 0.85 and 0.80),
247 respectively (Fig. 4b). These scores are statistically significant at 95% confidence level by the
248 Mann-Whitney U-test. When the ROC and ROL scores are calculated at each model grid, the
249 scores are higher than 0.5 in most summer rainfall regions of southern Africa except for
250 northeastern South Africa (Figs. 5 and 6). Moreover, areas with the ROC and ROL scores
251 above 0.7 are mostly confined to the northwestern and central parts of southern Africa. This is
252 in accordance with the areas of the highest ACCs (Fig. 3), suggesting the consistency among
253 the different verification methods.

254 Figure 7 shows the reliability curves and frequency histograms of the forecast
255 probabilities for the above- and below-normal precipitation. The regression lines weighted by
256 the frequency of forecast probabilities for the reliability curves are also superimposed. We
257 note that the 27-year probabilistic forecasts for precipitation anomalies at each of 221 model
258 grids in the southern African region of interest are included for the reliability examination,

259 and the sample size is thus increased to 5967. It is shown that the reliability curves for both
260 the above- and below-normal precipitation are below (above) the diagonal line at the high
261 (low) end of the forecast probabilities, indicating that the above- and below-normal
262 precipitation occur less (more) frequently than predicted. Moreover, the forecast probabilities
263 do not span much away from 33%, the climatological probability. These are common
264 problems suffered by many CGCMs in predicting the southern African summer precipitation
265 and need to be addressed in the future (e.g., Landman and Beraki 2012; Landman et al. 2012).

266

267 **4. Large-scale circulation anomalies related to the above/below-normal** 268 **precipitations and possible sources of predictability**

269 In light of the good skill in predicting the southern African precipitation anomalies in
270 DJF, we use the present model to investigate the relevant large-scale circulation anomalies
271 and possible sources of predictability. As indicated in Fig. 2, the model successfully predicts
272 five (six) of the total nine years in the above (below)-normal precipitation tercile. Those five
273 (six) years are 1988/1989, 1995/1996, 1999/2000, 2005/2006 and 2007/2008 (1982/1983,
274 1986/1987, 1991/1992, 1994/1995, 2000/2001 and 2006/2007). We have constructed DJF
275 composites for the successfully predicted years, and discuss possible reasons why the
276 prediction fails in the remaining years. Since qualitatively the same results are obtained even
277 if we use the GPCC and ARC2, we only present results from the GPCP in this section.

278 Positive (negative) precipitation anomalies are observed in vast areas of southern Africa
279 south (north) of 15°S in the successfully predicted above-normal precipitation years (Fig. 8a).
280 This indicates a southward shift of the inter-tropical convergence zone and it may be

281 associated with weakening and a southward shift of the South Atlantic and Indian Ocean
282 subtropical highs (Figs. 9a, c, e; Cook et al. 2004; Vignaud et al. 2009). Negative geopotential
283 height anomalies in the lower troposphere cover almost the whole southern African
284 subcontinent. The anomalous center in the southeastern Atlantic Ocean off the coast of
285 Namibia is related to anomalous moist westerlies and northwesterlies from the South Atlantic
286 Ocean to the subcontinent. In addition, the anomalous southeast-northwest pressure gradient
287 over southern Africa is conducive to anomalous moist northeasterlies and easterlies from the
288 western Indian Ocean to the subcontinent. As a result, the humidity in the lower troposphere
289 is increased significantly (Figs. 10a-c) and convections are enhanced (Figs. 11a-c), resulting
290 in more precipitation over southern Africa (Fig. 8a). Anomalies in the successfully predicted
291 below-normal years are close to a mirror image of the above (Figs. 8c, 9b, d, f, 10e-g, 11e-g).
292 Note that the anomalous patterns of atmospheric fields derived from the three reanalysis data
293 are qualitatively consistent, but show some differences on a local scale, especially in the
294 specific humidity and outgoing longwave radiation anomalies (Figs. 10-11). However, these
295 differences do not influence our conclusions.

296 The model predicts to some extent the weakening and southward shift of the South
297 Atlantic and Indian Ocean subtropical highs (Fig. 9g), the negative geopotential height
298 anomalies in the lower troposphere over southern Africa, and the anomalous center in the
299 southeastern Atlantic Ocean off Namibia. As a result, the anomalous northwesterlies and
300 westerlies from the South Atlantic Ocean to southern Africa, the increased specific humidity
301 in the lower troposphere (Fig. 10d), the enhanced convection (Fig. 11d), and positive
302 precipitation anomalies are also predicted reasonably well in the above-normal years (Fig. 8b).

303 However, the predicted cyclonic circulation anomalies in the southeastern Atlantic Ocean are
304 much weaker than the observed, and thus less moisture is fed from the South Atlantic to the
305 subcontinent. Also, the strong cyclonic circulation anomalies centered at around 35°E and
306 20°S (Fig. 9g) are prohibiting the anomalous moist westerlies and northwesterlies from the
307 Atlantic Ocean to extend eastward to the eastern part of southern Africa. This may lead to less
308 feeding of moisture to northeastern South Africa (Fig. 10d), less active convection (Fig. 11d)
309 and precipitation biases there (Figs. 8a-b). The forecasted precipitation and atmospheric
310 circulation anomalies in the successfully predicted below-normal years are almost a mirror
311 image of those in the successfully predicted above-normal years (Figs. 8d, 9h, 10h, 11h).

312 The circulation anomalies in the lower troposphere over southern Africa seen in the
313 successfully predicted above/below-normal precipitation years (Fig. 9) remind us of the
314 ENSO influence (e.g., Tyson and Preston-Whyte 2004). In fact, among the five successfully
315 predicted above-normal years, all have a distinct La Niña signal in the tropical Pacific, and
316 among six successfully predicted below-normal years, all but the 2000/2001 austral summer
317 have a distinct El Niño signal. As a result, composites of SST anomalies in these successfully
318 predicted years exhibit significant ENSO signals (Figs. 12a, c), and those of atmospheric
319 circulation anomalies (Fig. 9) are dominated by the ENSO-related teleconnections (Fig. 13). It
320 is not surprising that ENSO provides the dominant source of predictability. Landman and
321 Beraki (2012) also showed that their multi-model ensemble forecast system has better
322 prediction skills of southern African summer precipitation in the ENSO years than neutral
323 years. This is not only because of the close relation between ENSO and the southern African
324 summer precipitation, but also because ENSO itself is a highly predictable climate mode

325 providing dominant sources of predictability for the global climate variations. Hence, the high
326 prediction skills of the southern African summer precipitation in the SINTEX-F may be due
327 to its high skills predicting ENSO (Jin et al. 2008) and the associated large-scale
328 teleconnections in the Southern Hemisphere (Figs. 9g-h, 13g-h; Yuan et al. 2013). A separate
329 100-year control experiment confirms the robustness of the above relationship in the
330 SINTEX-F; the above (below)-normal precipitation in southern Africa is associated with La
331 Niña (El Niño) (figure not shown).

332 However, the model is over-confident in simulating the link between ENSO and
333 southern African summer precipitation. The correlation coefficient between the predicted
334 Niño-3 and southern African precipitation indices in DJF is -0.77, which is higher than -0.57
335 in the observation. This may explain why 1997/1998 is predicted as the driest summer in
336 association with the strongest 1997/1998 El Niño event even though it was not accompanied
337 by the driest summer in subtropical southern Africa (Lyon and Mason 2007).

338 Also, the model shows some biases in simulating the relationship on a local scale. As
339 shown in Figs. 14a and d, the observed precipitation anomalies over northeastern South Africa
340 in DJF are negatively correlated with ENSO, but they are positively correlated in the model.
341 This is probably because of model biases in circulation anomalies in the lower troposphere
342 associated with La Niña (El Niño); cyclonic (anticyclonic) circulation anomalies in the
343 southeastern Atlantic Ocean are too weak and cyclonic (anticyclonic) circulation anomalies
344 over southern Africa centered at around 35°E and 20°S are too strong in the model (Fig. 13).
345 We have discussed above that this may cause the precipitation biases in northeastern South
346 Africa and result in the lower prediction skills there (Figs. 3, 5-6).

347 There may be other sources of predictability beside ENSO, because significant SST
348 anomalies are found outside of the tropical eastern Pacific (Fig. 12). The SST anomalies along
349 the coast of Angola and Namibia are associated with Benguela Niño, which is closely related
350 to precipitation anomalies in the western part of southern Africa (Rouault et al. 2003;
351 Florenchie et al. 2003). Since it is predicted relatively well in the 1990s, it may partly explain
352 the better prediction skills in this decade when the correlation between ENSO and the
353 southern African summer precipitation is relatively weak (Fig. 15).

354 Also, the basin-wide cooling (warming) in the tropical Indian Ocean in the above
355 (below)-normal precipitation years (Fig. 12) may modulate the moisture fluxes from the
356 Indian Ocean to southern Africa and contribute to positive (negative) precipitation anomalies
357 (Goddard and Graham 1999). Although these SST anomalies are induced by ENSO through
358 an atmospheric bridge (e.g., Klein et al. 1999; Xie et al. 2009), they are essential to simulate
359 the correct precipitation response to ENSO in southern Africa (Goddard and Graham 1999).

360 In addition, Fig. 12 shows SST anomalies in the South Atlantic and the southern Indian
361 Ocean associated with the subtropical dipole modes. It is not clear to which extent the
362 subtropical dipole modes can provide an additional independent source of predictability for
363 the summer precipitation, since the subtropical dipole modes are related to ENSO (e.g.,
364 Hermes and Reason 2005; Yuan et al. 2013; Morioka et al. 2013). The correlation coefficient
365 between the Niño-3 and South Atlantic (Indian Ocean) subtropical dipole indices in DJF is
366 -0.59 (-0.35) for the observation and -0.55 (-0.36) for the model. These correlations are
367 significant at 95% confidence level. Here, the subtropical dipole mode indices are defined as
368 the difference in SST anomalies between the southwestern and northeastern poles as in Yuan

369 et al. (2013). Therefore, the correlation coefficients between the subtropical dipole modes and
370 precipitation anomalies are similar to those between the ENSO and precipitation anomalies
371 with opposite signs in both the observation (Figs. 14a-c) and the model (Figs. 14d-f).
372 Nevertheless, successful predictions of the subtropical dipole modes are important, because
373 some impacts of ENSO on the southern African summer precipitation may be through the
374 subtropical dipole modes via changing intensity and frequency of the synoptic rain-bearing
375 systems (Pohl et al. 2009; Vigaud et al. 2012).

376 The coupled model successfully predicts the La Niña Modoki in the tropical Pacific and
377 the below-normal precipitations in southern Africa in the austral summer of 2000/2001.
378 According to Ratnam et al. (2013a), La Niña Modoki is associated with the negative, though
379 not statistically significant, precipitation anomalies in South Africa. Hence, if the ENSO
380 Modoki is successfully predicted, it may provide an additional source of predictability for the
381 southern African summer precipitation.

382 There are three below-normal precipitation years that the model fails to predict
383 (1983/1984, 1989/1990 and 2002/2003). Although these years are not dry enough to become
384 the nine driest years (Fig. 2), they are predicted as the 12th, 13th and 11th driest years,
385 respectively. Among the four above-normal precipitation years that the model fails to predict
386 (1987/1988, 1990/1991, 1993/1994 and 2008/2009), 1993/1994 and 2008/2009 are predicted
387 as the 10th and 12th wettest years. In the austral summer of 1987/1988, the observed El Niño
388 decayed quickly in the tropical Pacific, but the predicted El Niño lasts much longer, resulting
389 in the dominant El Niño-related circulation anomalies over southern Africa and the 10th driest
390 summer in the model. Although 1990/1991 was an El Niño Modoki year, the model predicts

391 for a canonical El Niño year and thus negative precipitation anomalies over southern Africa.

392

393 **5. Discussions**

394 To check whether prediction skills vary during the wet season of southern Africa
395 generally spanning from October to the following April, we have calculated ACCs of
396 three-month precipitation anomalies at various lead times (Fig. 16). By no surprise,
397 precipitation anomalies in DJF are most predictable (Figs. 16i-l). This is expected because the
398 atmospheric circulation over southern Africa is predominantly influenced by the tropics in
399 DJF, and thus the potential predictability of precipitation is highest (e.g., Landman and Mason
400 1999; Landman et al. 2009). The figure also suggests that predictions initialized on October
401 1st have much better skills than those initialized on September 1st (Figs. 10k-l). Besides the
402 shorter lead-time, the initial information at the beginning of October may be important for a
403 coupled model to predict the onset of the wet season; it usually starts in October, but it is
404 difficult to simulate by general circulation models (Tozuka et al. 2013). On the other hand, the
405 prediction skills are not much different with initialization dates of October, November and
406 December 1st (Figs. 10i-k). This may be because ENSO, which provides the major source of
407 predictability, is consistently well predicted. The ACCs of Niño-3 index in DJF are almost the
408 same with 0.95 (± 0.02) for predictions initialized on October, November and December 1st.

409 On regional scale, the highest ACCs are confined to the western and central parts of
410 southern Africa, while low ACCs are found in northeastern South Africa. The low prediction
411 skills in the latter may be partly due to the model biases in the ENSO-related teleconnections.
412 In addition, they may be partly attributable to the coarse model resolution. The precipitation

413 in northeastern South Africa is strongly influenced by the escarpment (Garstang et al. 1987),
414 but the SINTEX-F is too coarse to realistically represent this complex topography. For this
415 reason, Ratnam et al. (2013b) recently used a regional model with horizontal resolution of 30
416 km to dynamically downscale prediction results from the SINTEX-F, and achieved better
417 prediction skills in northeastern South Africa.

418

419 **6. Conclusions**

420 We have assessed skills of the SINTEX-F coupled model in predicting the summer
421 precipitation in southern Africa (16°-33°E and 22°S-35°S) for the period of 1982-2008, and
422 discussed possible sources of predictability. The ACCs of southern African precipitation
423 indices in DJF are 0.68, 0.67 and 0.61, respectively, when the deterministic forecasts
424 initialized on October 1st are verified against GPCP, GPCC and ARC2. These are significant
425 at 99.95% confidence level by the one-tailed *t*-test, and higher than the 0.6 threshold value of
426 high prediction skills for seasonal precipitation (Marengo et al. 2005). The leave-one-out
427 cross-validated ROC scores for the probabilistic forecasts of the above (below)-normal
428 precipitation are 0.76, 0.76 and 0.80 (0.79, 0.82 and 0.78), respectively, when verified against
429 GPCP, GPCC and ARC2. The corresponding ROL scores are 0.84, 0.84 and 0.80 (0.85, 0.85
430 and 0.80), respectively. These scores are significant at 95% confidence level by the
431 Mann-Whitney U-test.

432 On a local scale, the model has the highest prediction skills in the western and central
433 parts of southern Africa, while skills are lower in northeastern South Africa. The lower
434 prediction skills in the latter region may be related to the model biases in the ENSO-related

435 teleconnections in the southern African region. Also, the coarse model resolution may
436 contribute to the lower skills, because the model cannot resolve the complex topography in
437 northeastern South Africa that is crucial for the deep convection in austral summer (Garstang
438 et al. 1987).

439 When prediction skills are evaluated for the whole wet season of southern Africa from
440 October to the following April, we have found that precipitation anomalies in DJF are most
441 predictable. This is consistent with the prevalent view that the atmospheric circulation over
442 southern Africa in DJF is predominantly influenced by the tropics, and thus the potential
443 predictability is highest.

444 It is shown that ENSO provides the dominant source of predictability. Among the five
445 above-normal precipitation years that are successfully predicted by the model initialized on
446 October 1st, all have distinct La Niña signals in the tropical Pacific, and among the six
447 successfully predicted below-normal years, five have distinct El Niño signals. Hence, the high
448 skills of the SINTEX-F model in predicting the southern African summer precipitation may
449 be due to the high predictability of ENSO (Luo et al. 2008; Jin et al. 2008) and the robust
450 ENSO-southern African summer precipitation relationship. However, the model is
451 over-confident in simulating the relationship.

452 Besides ENSO, the Benguela Niño may contribute to better prediction skills, especially
453 in the 1990s. The basin-wide SST anomalies in the tropical Indian Ocean and the subtropical
454 dipole modes in the South Atlantic and the southern Indian Ocean may provide additional
455 sources of predictability, although they are not totally independent of ENSO (Fig. 14; Hermes
456 and Reason 2005; Yuan et al. 2013; Morioka et al. 2013). Also, we cannot exclude other

457 sources of predictability such as the ENSO Modoki in the tropical Pacific; the model
458 successfully predicts the below-normal precipitation in southern Africa in the austral summer
459 of 2000/2001 probably due to a successful prediction of La Niña Modoki and its
460 teleconnection (Ratnam et al. 2013a).

461 The present study has provided promising results for seasonal prediction of
462 precipitation anomalies in the extratropics, where seasonal forecasts are considered difficult.
463 This encourages us to further downscale the model outputs by using a regional model
464 (Ratnam et al. 2013b) so that seasonal forecast information may be more readily used. A
465 real-time dynamical downscaling seasonal forecast for the southern African precipitation is
466 carried out in our group for the societal applications.

467

468 **Acknowledgments**

469 Constructive comments provided by two anonymous reviewers helped us to improve
470 the earlier manuscript. The SINTEX-F model was run on the Earth Simulator of Japan
471 Agency for Marine-Earth Science and Technology. The ARC2 data is downloaded from the
472 data library of the International Research Institute for Climate and Society. The present
473 research is supported by the Japan Science and Technology Agency (JST) and Japan
474 International Cooperation Agency (JICA) through Science and Technology Research
475 Partnership for Sustainable Development (SATREPS).

476

477 **References**

- 478 Adler, RF, Huffman GJ, Chang A, Ferraro R, Xie P, Janowiak J, Rudolf B, Schneider U,
479 Curtis S, Bolvin D, Gruber A, Susskind J, and Arkin P (2003) The Version 2 Global
480 Precipitation Climatology Project (GPCP) monthly precipitation analysis (1979-Present).
481 J Hydrometeor 4:1147-1167
- 482 Barnston AG, Thiao W, Kumar V (1996) Long-lead forecasts of seasonal precipitation in
483 Africa using CCA. Weather Forecast 11:506-520
- 484 Barnston AG, Tippett MK, L'Heureux ML, Li S, DeWitt DG (2012) Skill of real-time
485 seasonal ENSO model predictions during 2002-11. Bull Amer Meteor Soc 93:631-651
- 486 Behera SK, Yamagata T (2001) Subtropical SST dipole events in the southern Indian Ocean.
487 Geophys Res Lett 28:327–330
- 488 Boulard D, Pohl B, Crétat J, Vigaud N, Pham-Xuan T (2013) Downscaling large-scale climate
489 variability using a regional climate model: The case of ENSO over southern Africa.
490 Clim Dyn 40:1141-1168
- 491 Crétat J, Pohl B, Richard Y, Drobinski P (2012) Uncertainties in simulating regional climate
492 of southern Africa: Sensitivity to physical parameterizations using WRF. Clim Dyn
493 38:613-634
- 494 Conway G (2009) The science of climate change in Africa: Impacts and adaptation.
495 Discussion Paper No. 1, Grantham Institute for Climate Change, Imperial College
496 London, London, United Kingdom
- 497 Cook KH (2000) The South Indian Convergence Zone and interannual rainfall variability over
498 southern Africa. J Clim 13:3789-3804

499 Cook C, Reason CJC, Hewitson BC (2004) Wet and dry spells within particularly wet and dry
500 summers in the South African summer rainfall region. *Clim Res* 26:17-31

501 Dee DP and Coauthors (2011) The ERA-Interim reanalysis: Configuration and performance
502 of the data assimilation system. *Q J R Meteorol Soc* 137:553-597

503 Dyer TGJ (1979) Rainfall along the east coast of Southern Africa, the southern oscillation and
504 the latitude of the subtropical high pressure belt. *Q J R Meteorol Soc* 105:445-451

505 Fauchereau N, Pohl B, Reason CJC, Rouault M, Richard Y (2009) Recurrent daily OLR
506 patterns in the southern Africa/southwest Indian Ocean region, implication for South
507 African rainfall and teleconnections. *Clim Dyn* 32:575–591

508 Florenchie P, Lutjeharms JRE and Reason CJC (2003) The source of Benguela Niño in the
509 South Atlantic Ocean. *Geophys Res Lett* 30. doi:10.1029/2003GL017172

510 Garstang M, Kelbe BE, Emmitt GD, London WB (1987) Generation of convective storms
511 over the escarpment of northeastern South Africa. *Mon Weather Rev* 115:429-443

512 Goddard L and Graham NE (1999) Importance of the Indian Ocean for simulating rainfall
513 anomalies over eastern and southern Africa. *J Geophys Res* 104:19099-19116

514 Hagedorn R, Doblas-Reyes FJ, Palmer TN (2005) The rationale behind the success of
515 multi-model ensembles in seasonal forecasting – I. Basic concept. *Tellus* 57A:219-233

516 Harrison MSJ (1984) A generalized classification of South African summer rain-bearing
517 synoptic systems. *J Climatol* 4:547-560

518 Hart NCG, Reason CJC, Fauchereau N (2010) Tropical-extratropical interactions over
519 southern Africa: Three cases of heavy summer season rainfall. *Mon Weather Rev*
520 138:2608-2623

521 Hart NCG, Reason CJC, Fauchereau N (2012) Building a tropical-extratropical cloud band
522 metbot. *Mon Weather Rev* 140:4005-4016

523 Hermes JC and Reason CJC (2005) Ocean model diagnosis of interannual coevolving SST
524 variability in the South Indian and South Atlantic Oceans. *J Clim* 18:2864-2882

525 Jin EK, Kinter L III, Wang B, Kang IS, Shukla J, Kirtman BP, Kug JS, Yamagata T, Luo JJ,
526 Schemm J, Kumar A (2008) Current status of ENSO prediction skill in coupled
527 ocean-atmosphere models. *Clim Dyn* 31: 647-664

528 Joubert AM (1997) Simulations by the atmospheric model intercomparison project of
529 atmospheric circulation over southern Africa. *Int J Climatol* 17:1129-1154

530 Kalnay E and Coauthors (1996) The NCEP/NCAR 40-year reanalysis project. *Bull Amer*
531 *Meteor Soc* 77:437-471

532 Kataoka T, Tozuka T, Masumoto Y, Yamagata T (2012) The Indian Ocean subtropical dipole
533 mode simulated in the CMIP3 models. *Clim Dyn* 39:1385-1399

534 Kirtman BP, Shukla J, Huang B, Zhu Z, Schneider EK (1997) Multiseasonal predictions with
535 a coupled tropical ocean-global atmosphere system. *Mon Weather Rev* 125:789-808

536 Klein SA, Soden BJ, Lau NC (1999) Remote sea surface temperature variations during
537 ENSO: Evidence for a tropical atmospheric bridge. *J Clim* 12:917-932

538 Landman WA, Beraki A (2012) Multi-model forecast skill for mid-summer rainfall over
539 southern Africa. *Int J Climatol* 32:303-314

540 Landman WA, DeWitt D, Lee DE, Beraki A, Lötter D (2012) Seasonal rainfall prediction

541 skill over South Africa: One- versus two-tiered forecasting systems. *Weather Forecast*
542 27:489-501

543 Landman WA, Goddard L (2002) Statistical recalibration of GCM forecasts over southern
544 Africa using model output statistics. *J Clim* 15:2038-2055

545 Landman WA, Mason SJ (1999) Operational long-lead prediction of South African rainfall
546 using canonical correlation analysis. *Int J Climatol* 19:1073-1090

547 Landman WA, Mason SJ, Tyson PD, Tennant WJ (2001) Retroactive skill of multi-tiered
548 forecasts of summer rainfall over southern Africa. *Int J Climatol* 21:1-19

549 Lindesay JA (1988) South African rainfall, the Southern Oscillation, and a Southern
550 Hemisphere semi-annual cycle. *J Clim* 8:17-30

551 Love TB, Kumar V, Xie P, Thiaw W (2004) A 20-year daily Africa precipitation climatology
552 using satellite and gauge data. *Proceeding of the 84th AMS annual meeting, Seattle,*
553 *Washington.*

554 Luo JJ, Masson S, Behera SK, Gualdi S, Navarra A, Yamagata T (2003) South Pacific origin
555 of the decadal ENSO-like variation as simulated by a coupled GCM. *Geophys Res Lett*
556 30. doi:10.1029/2003GL018649

557 Luo JJ, Masson S, Roeckner E, Madec G, Yamagata T (2005a) Reducing climatology bias in
558 an ocean-atmosphere CGCM with improved coupling physics. *J Clim* 18:2344–2360

559 Luo JJ, Masson S, Behera SK, Shingu S, Yamagata T (2005b) Seasonal climate predictability
560 in a coupled AOGCM using a different approach for ensemble forecast. *J Clim*
561 18:4474-4497

562 Luo JJ, Masson S, Behera SK, Yamagata T (2007) Experimental forecasts of the Indian

563 Ocean Dipole using a coupled OAGCM. *J Clim* 20:2178–2190

564 Luo JJ, Masson S, Behera SK, Yamagata T (2008) Extended ENSO predictions using a fully
565 coupled ocean-atmosphere model. *J Clim* 21:84–93

566 Lyon B, Mason SJ (2007) The 1997-98 summer rainfall season in southern Africa. Part I:
567 Observations. *J Clim* 20:5134-5148

568 Madec G, Delecluse P, Imbard M, Levy C (1998) OPA 8.1 ocean general circulation model
569 reference manual. Tech. Rep. Note 11, LODYC/IPSL, Paris, France

570 Marengo J, Alves LM, Camargo H (2005) Global climate predictability at seasonal to
571 interannual time scales. *GEWEX News*, Vol. 15, No.4, International GEWEX Project
572 Office, Silver Spring, MD, 6-7

573 Mason SJ (1995) Sea-surface temperature-South African rainfall associations, 1910-1989. *Int*
574 *J Climatol* 15:119–135

575 Mason SJ, Graham NE (1999) Conditional probabilities, relative operating characteristics, and
576 relative operating levels. *Weather Forecast* 14:713-725

577 Mason SJ, Graham NE (2002) Areas beneath the relative operating characteristics (ROC) and
578 relative operating levels (ROL) curves: Statistical significance and interpretation. *Q J R*
579 *Meteorol Soc* 128:2145-2166

580 Mason SJ, Joubert AM, Cosijn C, Crimp SJ (1996) Review of seasonal forecasting techniques
581 and their applicability of southern Africa. *Water SA* 22:203-209

582 Morioka Y, Tozuka T, Yamagata T (2010) Climate variability in the southern Indian Ocean as
583 revealed by self-organizing maps. *Clim Dyn* 35:1059–1072

584 Morioka Y, Tozuka T, Yamagata T (2011) On the growth and decay of the subtropical dipole

585 mode in the South Atlantic. *J Clim* 24:5538–5554

586 Morioka Y, Tozuka T, Yamagata T (2013) How is the Indian Ocean subtropical dipole
587 excited? *Clim Dyn*. doi: 10.1007/s00382-012-1584-9

588 Pohl B, Fauchereau N, Richard Y, Rouault M, Reason CJC (2009) Interactions between
589 synoptic, intraseasonal and interannual convective variability over southern Africa.
590 *Clim Dyn* 33:1033-1050

591 Ratna SB, Behera SK, Ratnam JV, Takahashi K, Yamagata T (2012) An index for tropical
592 temperate troughs over southern Africa. *Clim Dyn*. doi:10.1007/s00382-012-1540-8

593 Ratnam JV, Behera SK, Masumoto Y, Takahashi K, Yamagata T (2012) A simple regional
594 coupled model experiment for summer-time climate simulation over southern Africa.
595 *Clim Dyn* 39:2207-2217

596 Ratnam JV, Behera SK, Masumoto Y, Yamagata T (2013a) Tropical Pacific influences on the
597 austral summer precipitation of southern Africa. *Clim Dyn* (in revision)

598 Ratnam JV, Behera SK, Ratna SB, Rautenbach CJ, Lennard C, Luo JJ, Masumoto Y,
599 Takahashi K, Yamagata T (2013b) Dynamical downscaling of austral summer climate
600 forecasts over southern Africa using a regional coupled model. *J Clim* (submitted)

601 Reason CJC (2001) Subtropical Indian Ocean dipole events and southern African rainfall.
602 *Geophys Res Lett* 28:2225–2227

603 Reason CJC (2002) Sensitivity of the southern African circulation to dipole sea-surface
604 temperature patterns in the South Indian Ocean. *Int J Climatol* 22:377-393

605 Reason CJC, Allan RJ, Lindesay JA, Ansell TJ (2000) ENSO and climatic signals across the
606 Indian Ocean basin in the global context: Part 1, interannual composite patterns. *Int J*

607 Climatol 20:1285-1327

608 Reason CJC, Jagadheesha D (2005) Relationships between South Atlantic SST variability and
609 atmospheric circulation over the South African region during austral winter. J Clim
610 18:3339-3355

611 Reason CJC, Keibel A (2004) Tropical cyclone Eline and its unusual penetration and impacts
612 over the southern Africa. Weather Forecast 19:789-805

613 Reason CJC, Rouault M (2002) ENSO-like decadal patterns and South African rainfall.
614 Geophys Res Lett 29. doi:10.1029/2002GL014663

615 Reynolds RW, Rayner NA, Smith TM, Stokes DC, Wang W (2002) An improved in situ and
616 satellite SST analysis for climate. J Clim 15:1609–1625

617 Richard Y, Trzaska S, Roucou P, Rouault M (2000) Modification of the southern African
618 rainfall variability/ENSO relationship since the late 1960s. Clim Dyn 16:883-895

619 Roeckner E, Arpe K, Bengtsson L, Christoph M, Claussen M, Dümenil L, Esch M, Giorgetta
620 M, Schlese U, Schulzweida U (1996) The atmospheric general circulation model
621 ECHAM-4: Model description and simulation of present-day climate. Tech. Rep. No.
622 218, Max-Planck-Institut für Meteorologie, Hamburg, Germany

623 Rouault M, Florenchie P, Fauchereau N, Reason CJC (2003) South East tropical Atlantic
624 warm events and southern African rainfall. Geophys Res Lett 30.
625 doi:10.1029/2002GL014840

626 Rouault M, Richard Y (2005) Spatial extent and intensity of droughts in southern Africa.
627 Geophys Res Lett 32. doi:10.1029/2005GL022436

628 Saha S and Coauthors (2010) The NCEP climate forecast system reanalysis. Bull Amer

629 Meteor Soc 91:1015-1057

630 Schneider U, Becker A, Finger P, Meyer-Christoffer A, Xiese M, Rudolf B (2013) CGPP's
631 new land surface precipitation climatology based on quality-controlled in situ data and
632 its role in quantifying the global water cycle. Theor Appl Climatol.
633 doi:10.1007/s00704-013-0860-x

634 Todd MC, Washington R (1999) Circulation anomalies associated with tropical-temperate
635 troughs in southern Africa and the southwest Indian Ocean. Clim Dyn 15:937–951

636 Tozuka T, Luo JJ, Masson S, Behera SK, Yamagata T (2005) Annual ENSO simulated in a
637 coupled ocean-atmosphere model. Dyn Atmos Ocean 39:41–60

638 Tozuka T, Abiodun BJ, Engelbrecht FA (2013) Impacts of convection schemes on simulating
639 tropical-temperate troughs over southern Africa. Clim Dyn.
640 doi:10.1007/s00382-013-1738-4

641 Tyson PD, Preston-Whyte RA (2004) The weather and climate of southern Africa. Oxford
642 University Press, pp 232-244

643 Venegas SA, Mysak LA, Straub DN (1997) Atmosphere-ocean coupled variability in the
644 South Atlantic. J Clim 10:2904–2920

645 Vigaud N, Richard Y, Rouault M, Fauchereau N (2009) Moisture transport between the South
646 Atlantic Ocean and southern Africa: Relationships with summer rainfall and associated
647 dynamics. Clim Dyn 32:113–123

648 Vigaud N, Pohl B, Crétat J (2012) Tropical-temperate interactions over southern Africa
649 simulated by a regional climate model. Clim Dyn 39:2895-2916

650 Walker ND (1990) Links between South African summer rainfall and temperature variability
651 of the Agulhas and Benguela Current systems. *J Geophys Res* 95:3297-3319

652 Wilks DS (1995) *Statistical methods in the atmospheric sciences: An introduction*. Academic
653 Press, p 467.

654 Xie SP, Hu K, Hafner J, Tokinaga H, Du Y, Huang G, Sampe T (2009) Indian Ocean
655 capacitor effects on Indo-Western Pacific climate during the summer following El Niño.
656 *J Clim* 22:730-747

657 Yuan C, Tozuka T, Luo JJ, Yamagata T (2013) Predictability of subtropical dipole modes in a
658 coupled ocean-atmosphere model. *Clim Dyn*. doi:10.1007/s00382-013-1704-1

659

660 **Figure Captions**

661 **Figure 1:** Mean precipitation (shading, in mm day^{-1}) and moisture flux at 850 hPa (vector, in
662 $\text{kg m}^{-1} \text{s}^{-1}$) over southern Africa during DJF in (a) GPCP and NCEP/NCAR reanalysis 1,
663 (b) GPCC and ERA-Interim, (c) ARC2 and CFSR, and (d) ensemble-mean forecasts
664 initialized on October 1st for the period of 1982-2008. The white box in (a) denotes the
665 area used to define the southern African precipitation index in this study.

666 **Figure 2:** Time series of the southern African precipitation indices in DJF. Years in the x-axis
667 represent the three-month-mean period from December of that year till the following
668 February. Black (blue) solid line represents the index derived from GPCP
669 (ensemble-mean forecasts initialized on October 1st). Also shown are the
670 box-and-whisker plots for the nine ensemble members at each year; the red boxes
671 represent the interquartile ranges of the middle 56% ensemble members (five out of
672 nine members). Green horizontal bars within the red boxes indicate precipitation
673 anomalies of the median member, and red cross symbols show the maximum and
674 minimum precipitation anomalies from the nine members.

675 **Figure 3:** Anomaly correlation coefficients (ACCs) of the deterministic forecasts initialized
676 on October 1st for precipitation anomalies in DJF when verified against (a) GPCP, (b)
677 GPCC and (c) ARC2 for the period of 1982 to 2008. White dashed contours denote
678 ACCs of 0.32, significant at 95% confidence level by the one-tailed *t*-test.

679 **Figure 4:** Leave-one-out cross-validated (a) ROC and (b) ROL scores for the probabilistic
680 forecasts of (blue) above- and (red) below-normal southern African precipitation in
681 DJF. The probabilistic forecasts are initialized on October 1st and verified against

682 GPCP, GPCC and ARC2. The threshold value for above (below)-normal tercile is the
683 lowest (highest) value in the highest (lowest) 33% of the historical records. The score
684 of 0.7 is significant at 95% confidence level by the Mann-Whitney U-test.

685 **Figure 5:** Spatial distribution of the leave-one-out cross-validated ROC scores for the
686 probabilistic forecasts of (a-c) above- and (d-f) below-normal precipitation. The
687 forecasts are initialized on October 1st and verified against (a, d) GPCP, (b, e) GPCC
688 and (c, f) ARC2. The threshold value for above (below)-normal tercile is the lowest
689 (highest) value in the highest (lowest) 33% of the historical records. White dashed
690 contours denote the score of 0.7, which is significant at 95% confidence level by the
691 Mann-Whitney U-test.

692 **Figure 6:** As in Fig. 5, but for the leave-one-out cross-validated ROL scores.

693 **Figure 7:** Reliability diagrams and frequency histograms of the probabilistic forecasts
694 initialized on October 1st for (blue) above- and (red) below-normal precipitation over
695 southern Africa in DJF when verified against (a) GPCP, (b) GPCC and (c) ARC2. The
696 solid lines denote the reliability curves, the filled vertical bars the frequencies of
697 forecast probabilities, and the dotted lines the linear regression of the reliability curves
698 weighted by the frequencies of forecast probabilities. The threshold value for above
699 (below)-normal tercile is the lowest (highest) value in the highest (lowest) 33% of the
700 historical records.

701 **Figure 8:** Composites of precipitation anomalies (mm day^{-1}) in DJF for (a-b) above- and (c-d)
702 below-normal precipitation years that are successfully predicted by the model

703 initialized on October 1st. Here, (a, c) GPCP and (b, d) ensemble-mean forecasts are
704 used. The stippling denotes anomalies significant at 90% confidence level.

705 **Figure 9:** Composites of geopotential height (shading, in m) and wind (vector, in m s^{-1})
706 anomalies at 850 hPa in DJF for (a, c, e, g) above- and (b, d, f, h) below-normal
707 precipitation years that are successfully predicted by the model initialized on October
708 1st. Geopotential height anomalies significant at 90% confidence level are stippled and
709 only wind anomalies significant at 90% confidence level are shown. Here, (a, b)
710 NCEP/NCAR, (c, d) ERA-Interim, (e, f) CFSR and (g, h) ensemble-mean forecasts are
711 used.

712 **Figure 10:** Composites of the specific humidity anomalies (kg kg^{-1}) in (a-d) above- and (e-h)
713 below-normal precipitation years that are successfully predicted by the model
714 initialized on October 1st. Here, (a, e) NCEP/NCAR, (b, f) ERA-Interim, (c, g) CFSR
715 and (d, h) ensemble-mean forecasts are used. The stippling denotes anomalies
716 significant at 90% confidence level.

717 **Figure 11:** As in Fig. 10, but for outgoing longwave radiation anomalies (W m^{-2}).

718 **Figure 12:** As in Fig. 8, but for SST anomalies ($^{\circ}\text{C}$) in (a, c) OISST and (b, d) ensemble-mean
719 forecasts initialized on October 1st.

720 **Figure 13:** As in Fig. 9, but for the composites of (a, c, e, g) four La Niña and (b, d, f, h) four
721 El Niño during the period of 1982-2008. Here, 1984/1985, 1988/1989, 1999/2000, and
722 2009/2010 (1982/1983, 1986/1987, 1991/1992 and 1997/1998) are defined as La Niña
723 (El Niño) years following Ratnam et al. (2013a).

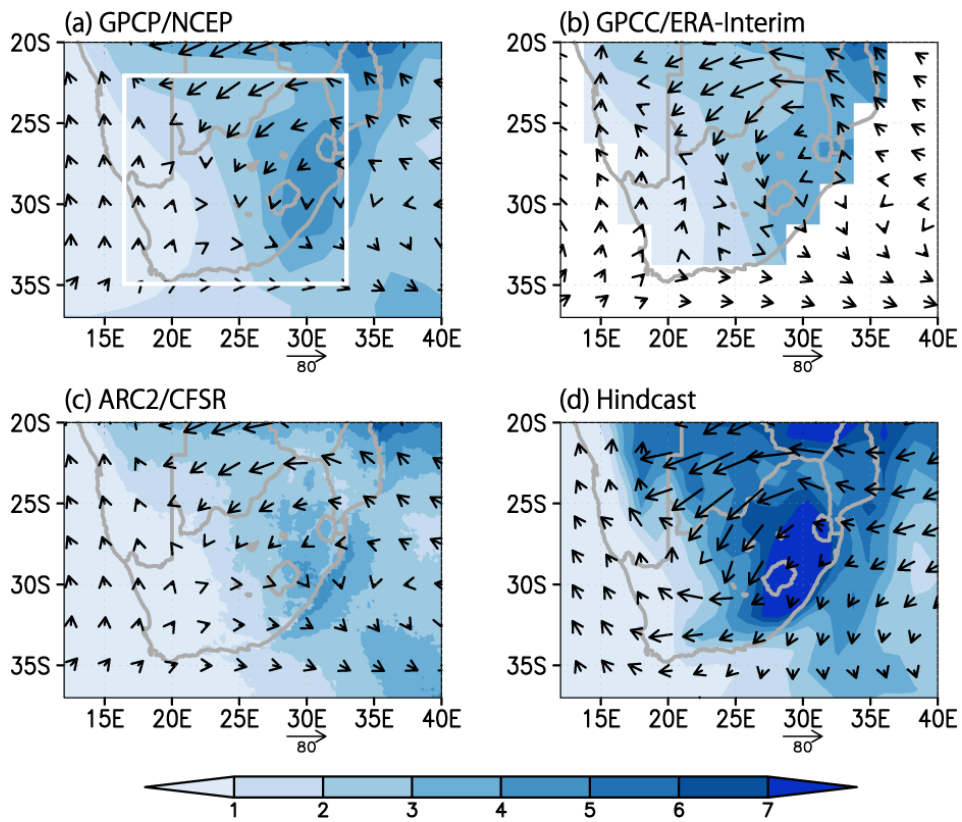
724 **Figure 14:** Observed and model correlation coefficients between precipitation anomalies and

725 (a, d) Niño-3, (b, e) South Atlantic subtropical dipole and (c, f) Indian Ocean
726 subtropical dipole indices in DJF for the period of 1982-2008. The precipitation and
727 SST data used are (a-c) OISST and GPCP and (d-f) ensemble-mean forecasts
728 initialized on October 1st.

729 **Figure 15:** Eleven-year sliding correlation coefficients between (black line) the observed and
730 predicted southern African summer precipitation indices in DJF, (blue line) the
731 observed and predicted Benguela Niño indices in DJF, and (red line) the observed
732 southern African precipitation and Niño-3 indices (multiplied by -1) in DJF. The year
733 in the x-axis represents the central year of the eleven-year sliding window. The
734 observed data used are GPCP and OISST and the forecasts are initialized on October
735 1st. The Benguela Niño index is defined as SST anomalies averaged from 10° to 20°S
736 and 8°E to the coast following Florenchie et al. (2003).

737 **Figure 16:** ACCs of 3-month-mean precipitation anomalies in southern Africa for (a-d)
738 October-December, (e-h) November-January, (i-l) December-February, (m-p)
739 January-March and (q-t) February-April. The forecasts are at (a, e, i, m, q) 1-3, (b, f, j,
740 n, r) 2-4, (c, g, k, o, s) 3-5 and (d, h, l, p, t) 4-6 months lead and the initialization dates
741 are shown on the top of each panel. The GPCP is used for verification. White dashed
742 contours denote ACCs of 0.32, significant at 95% confidence level by the one-tailed
743 *t*-test.

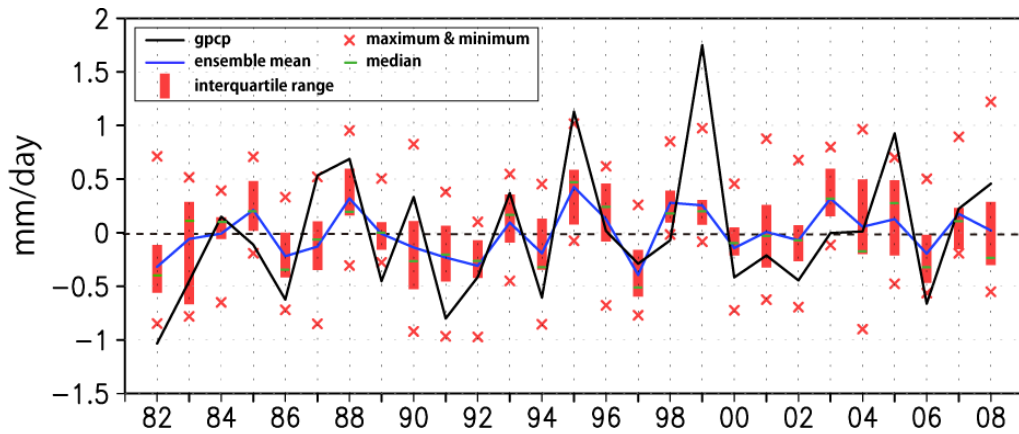
744



746

747 **Figure 1:** Mean precipitation (shading, in mm day^{-1}) and moisture flux at 850 hPa (vector, in
 748 $\text{kg m}^{-1} \text{s}^{-1}$) over southern Africa during DJF in (a) GPCP and NCEP/NCAR reanalysis 1, (b)
 749 GPCC and ERA-Interim, (c) ARC2 and CFSR, and (d) ensemble-mean forecasts initialized
 750 on October 1st for the period of 1982-2008. The white box in (a) denotes the area used to
 751 define the southern African precipitation index in this study.

752



753

754

Figure 2: Time series of the southern African precipitation indices in DJF. Years in the x-axis

755

represent the three-month-mean period from December of that year till the following February.

756

Black (blue) solid line represents the index derived from GPCP (ensemble-mean forecasts

757

initialized on October 1st). Also shown are the box-and-whisker plots for the nine ensemble

758

members at each year; the red boxes represent the interquartile ranges of the middle 56%

759

ensemble members (five out of nine members). Green horizontal bars within the red boxes

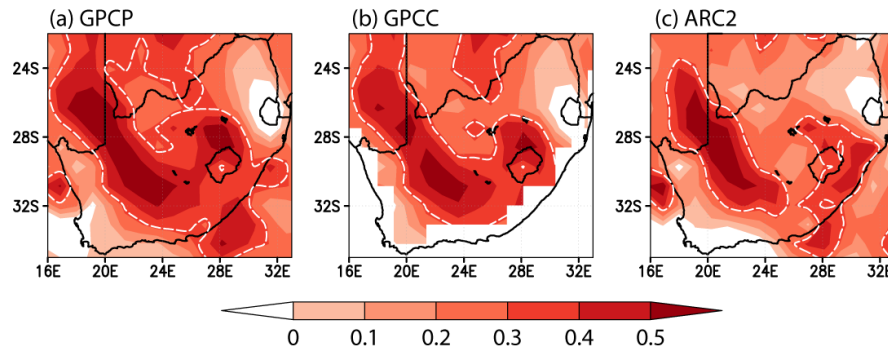
760

indicate precipitation anomalies of the median member, and red cross symbols show the

761

maximum and minimum precipitation anomalies from the nine members.

762



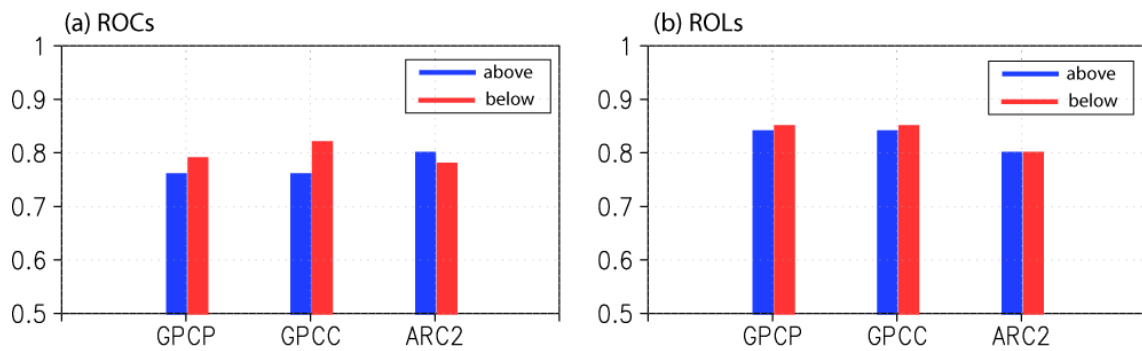
763

764 **Figure 3:** Anomaly correlation coefficients (ACCs) of the deterministic forecasts
 765 initialized on October 1st for precipitation anomalies in DJF when verified against (a)
 766 GPCP, (b) GPCC and (c) ARC2 for the period of 1982 to 2008. White dashed contours
 767 denote ACCs of 0.32, significant at 95% confidence level by the one-tailed *t*-test.

768

769

770

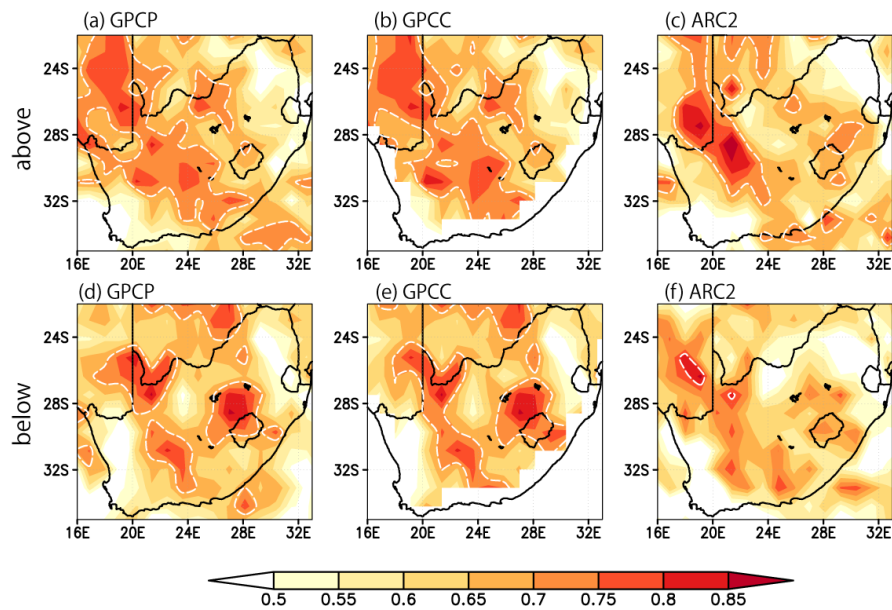


771

772 **Figure 4:** Leave-one-out cross-validated (a) ROC and (b) ROL scores for the
773 probabilistic forecasts of (blue) above- and (red) below-normal southern African
774 precipitation in DJF. The probabilistic forecasts are initialized on October 1st and
775 verified against GPCP, GPCC and ARC2. The threshold value for above
776 (below)-normal tercile is the lowest (highest) value in the highest (lowest) 33% values
777 of the historical records. The score of 0.7 is significant at 95% confidence level by the
778 Mann-Whitney U-test.

779

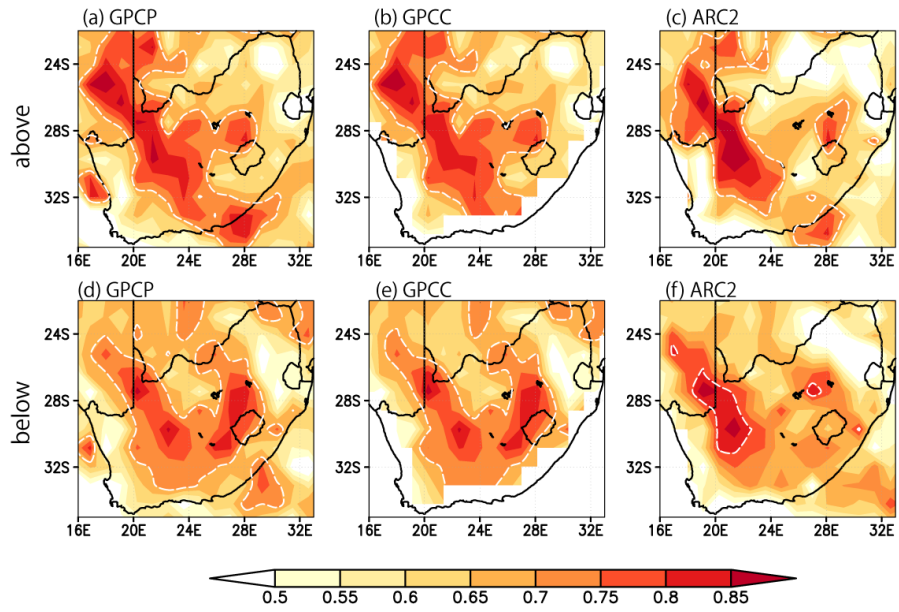
780



781

782 **Figure 5:** Spatial distribution of the leave-one-out cross-validated ROC scores for the
783 probabilistic forecasts of (a-c) above- and (d-f) below-normal precipitation. The
784 forecasts are initialized on October 1st and verified against (a, d) GPCP, (b, e) GPC
785 and (c, f) ARC2. The threshold value for above (below)-normal tercile is the lowest
786 (highest) value in the highest (lowest) 33% values of the historical records. White
787 dashed contours denote the score of 0.7, which is significant at 95% confidence level by
788 the Mann-Whitney U-test.

789



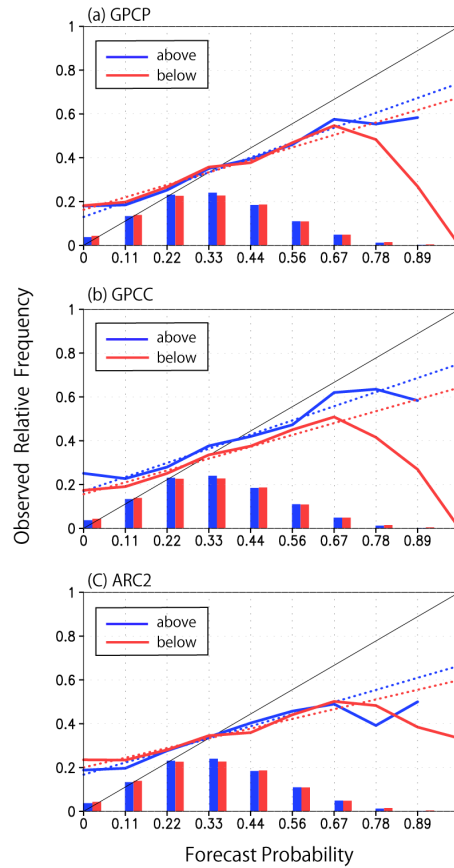
790

791 **Figure 6:** As in Fig. 5, but for the leave-one-out cross-validated ROL scores.

792

793

794



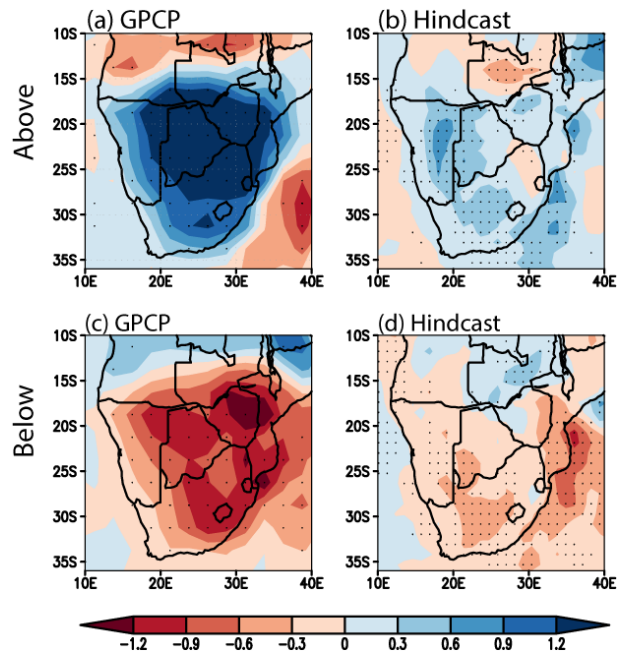
795

796 **Figure 7:** Reliability diagrams and frequency histograms of the probabilistic forecasts
797 initialized on October 1st for (blue) above- and (red) below-normal precipitation over southern
798 Africa in DJF when verified against (a) GPCP, (b) GPCP and (c) ARC2. The solid lines
799 denote the reliability curves, the filled vertical bars the frequencies of forecast probabilities,
800 and the dotted lines the linear regression of the reliability curves weighted by the frequencies
801 of forecast probabilities. The threshold value for above (below)-normal tercile is the lowest
802 (highest) value in the highest (lowest) 33% of the historical records.

803

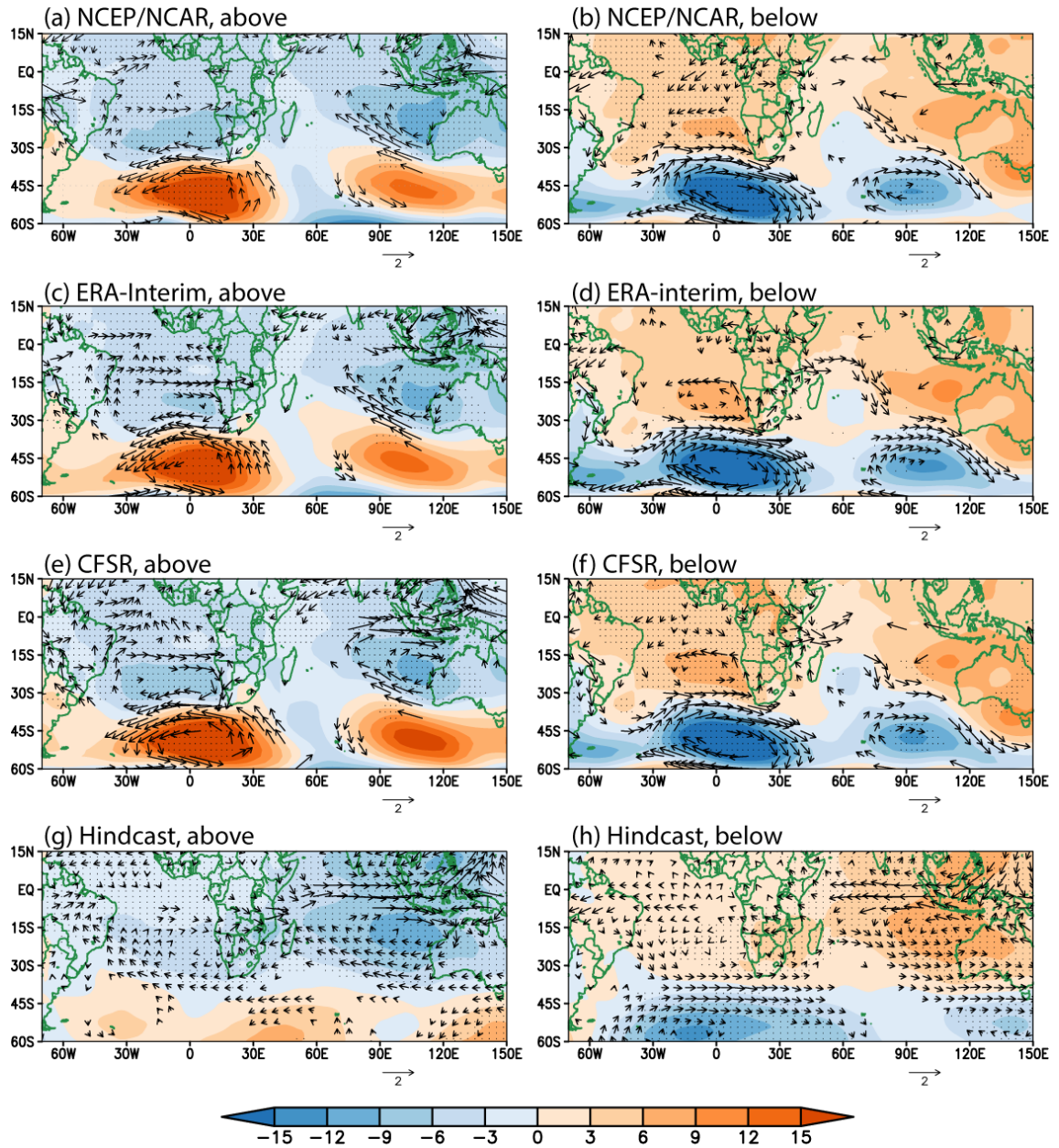
804

805



806

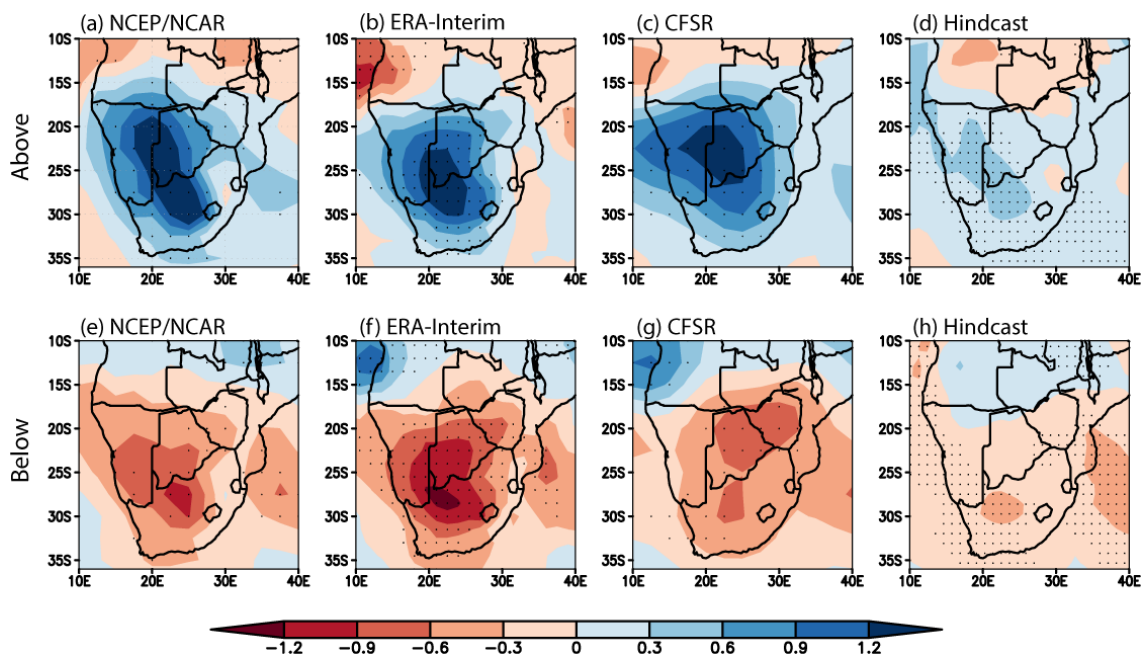
807 **Figure 8:** Composites of precipitation anomalies (mm day^{-1}) in DJF for (a-b) above- and (c-d)
 808 below-normal precipitation years that are successfully predicted by the model initialized on
 809 October 1st. Here, (a, c) GPCP and (b, d) ensemble-mean forecasts are used. The stippling
 810 denotes anomalies significant at 90% confidence level.



811

812 **Figure 9:** Composites of geopotential height (shading, in m) and wind (vector, in m s^{-1})
 813 anomalies at 850 hPa in DJF for (a, c, e, g) above- and (b, d, f, h) below-normal precipitation
 814 years that are successfully predicted by the model initialized on October 1st. Geopotential
 815 height anomalies significant at 90% confidence level are stippled and only wind anomalies
 816 significant at 90% confidence level are shown. Here, (a, b) NCEP/NCAR, (c, d) ERA-Interim,
 817 (e, f) CFSR and (g, h) ensemble-mean forecasts are used.

818
819
820

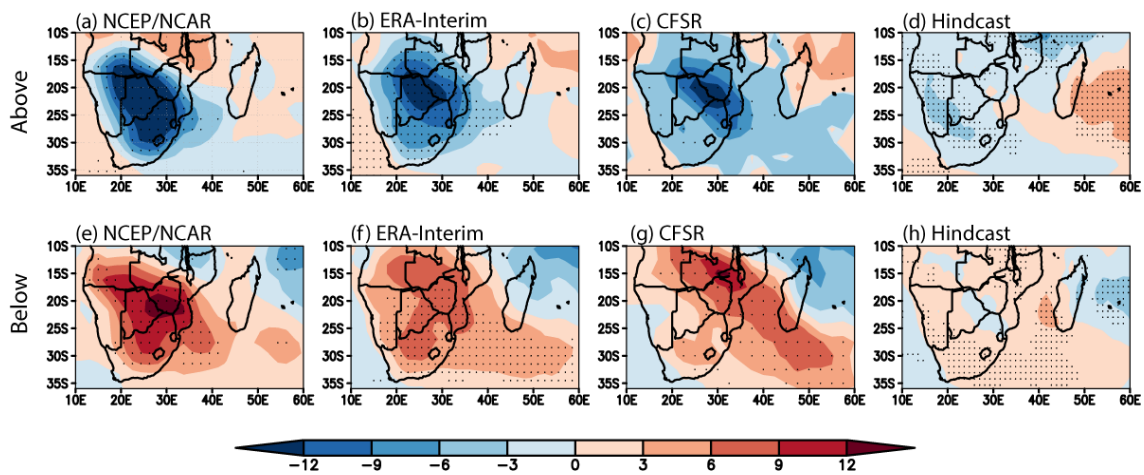


821

822 **Figure 10:** Composites of the specific humidity anomalies (kg kg^{-1}) in (a-d) above- and (e-h)
823 below-normal precipitation years that are successfully predicted by the model initialized on
824 October 1st. Here, (a, e) NCEP/NCAR, (b, f) ERA-Interim, (c, g) CFSR and (d, h)
825 ensemble-mean forecasts are used. The stippling denotes anomalies significant at 90%
826 confidence level.

827

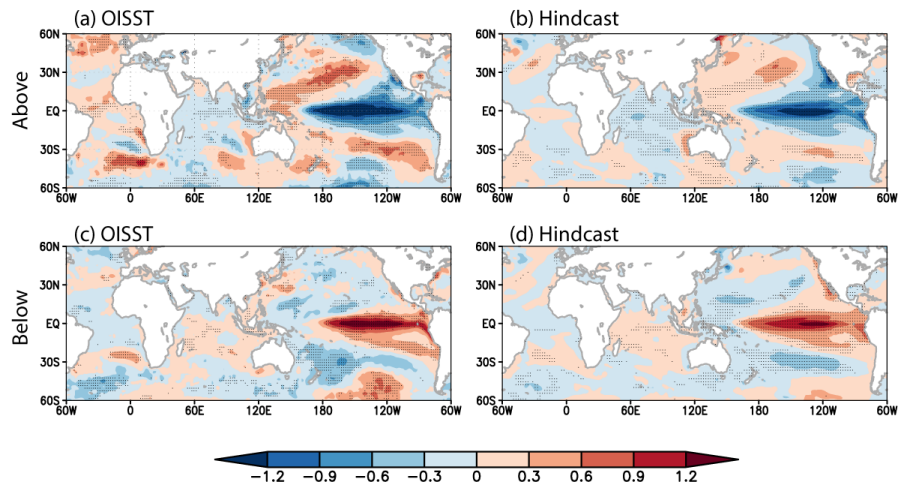
828



829

830 **Figure 11:** As in Fig. 10, but for outgoing longwave radiation anomalies ($W m^{-2}$).

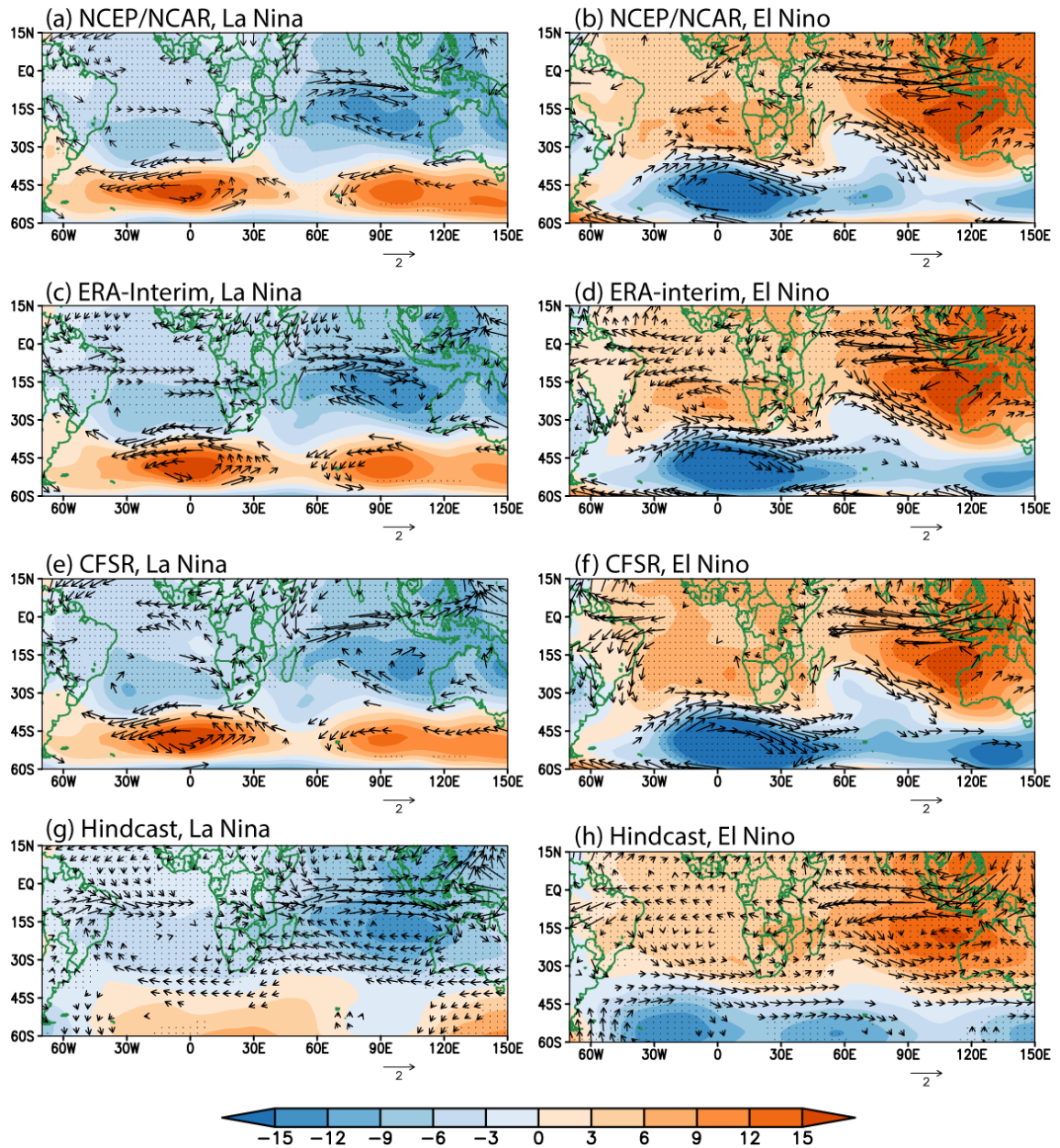
831



832

833 **Figure 12:** As in Fig. 8, but for SST anomalies ($^{\circ}\text{C}$) in (a, c) OISST and (b, d) ensemble-mean
834 forecasts initialized on October 1st.

835



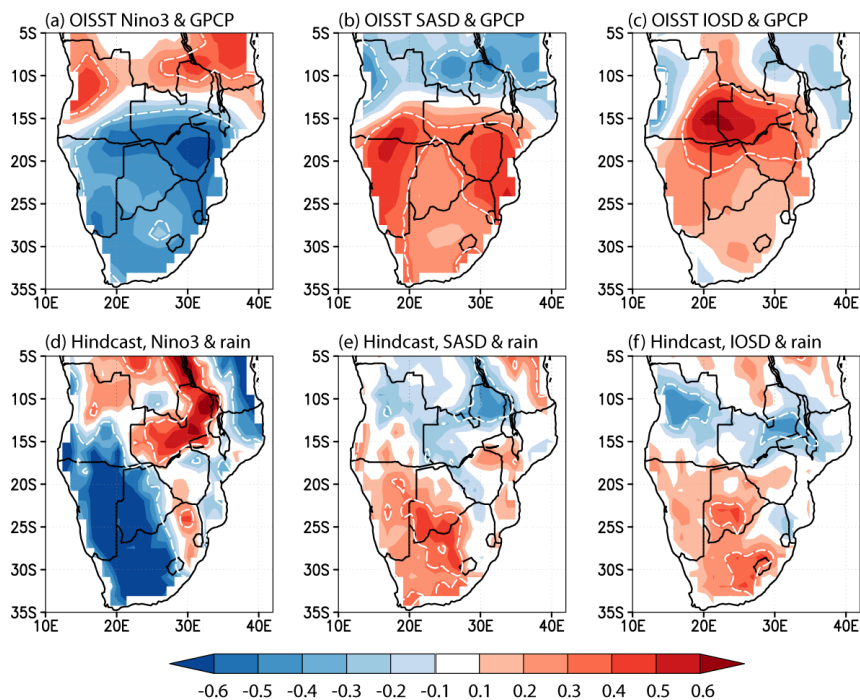
836

837 **Figure 13:** As in Fig. 9, but for the composites of (a, c, e, g) four La Niña and (b, d, f, h) four
 838 El Niño during the period of 1982-2008. Here, 1984/1985, 1988/1989, 1999/2000, and
 839 2009/2010 (1982/1983, 1986/1987, 1991/1992 and 1997/1998) are defined as La Niña (El
 840 Niño) years following Ratnam et al. (2013a).

841

842

843



844

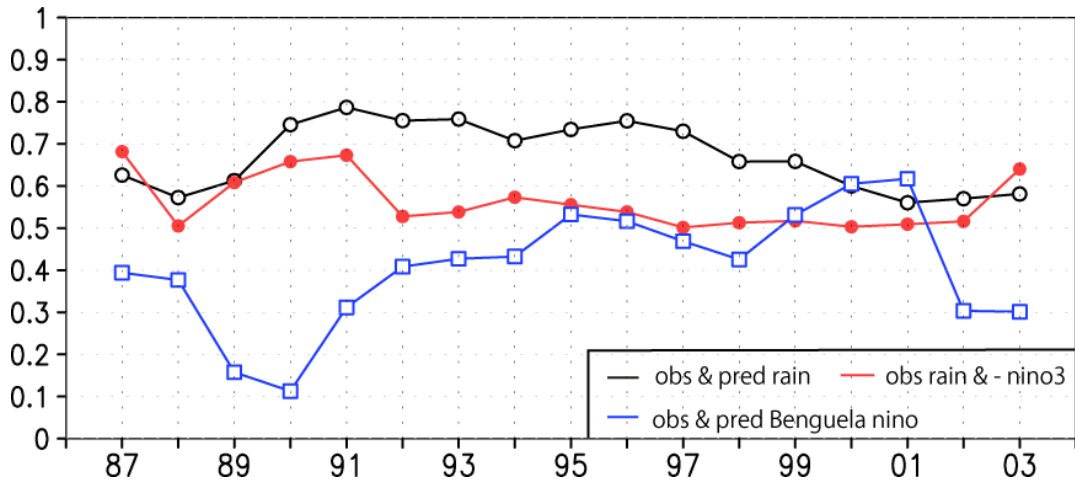
845 **Figure 14:** Observed and model correlation coefficients between precipitation anomalies and

846 (a, d) Niño-3, (b, e) South Atlantic subtropical dipole and (c, f) Indian Ocean subtropical

847 dipole indices in DJF for the period of 1982-2008. The precipitation and SST data used are

848 (a-c) OISST and GPCP and (d-f) ensemble-mean forecasts initialized on October 1st.

849



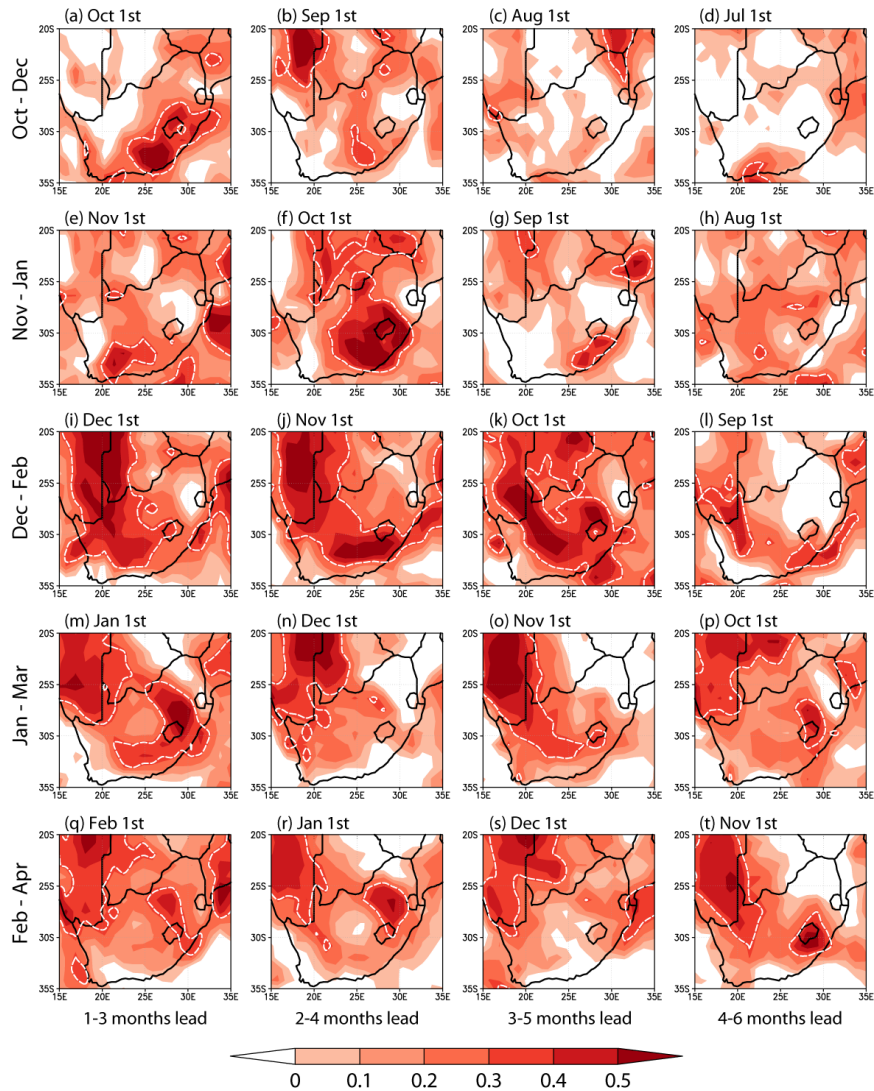
850

851 **Figure 15:** Eleven-year sliding correlation coefficients between (black line) the observed and
 852 predicted southern African summer precipitation indices in DJF, (blue line) the observed and
 853 predicted Benguela Niño indices in DJF, and (red line) the observed southern African
 854 precipitation and Niño-3 indices (multiplied by -1) in DJF. The year in the x-axis represents
 855 the central year of the eleven-year sliding window. The observed data used are GPCP and
 856 OISST and the forecasts are initialized on October 1st. The Benguela Niño index is defined as
 857 SST anomalies averaged from 10° to 20°S and 8°E to the coast following Florenchie et al.
 858 (2003).

859

860

861



862

863 **Figure 16:** ACCs of 3-month-mean precipitation anomalies in southern Africa for (a-d)
 864 October-December, (e-h) November-January, (i-l) December-February, (m-p) January-March
 865 and (q-t) February-April. The forecasts are at (a, e, i, m, q) 1-3, (b, f, j, n, r) 2-4, (c, g, k, o, s)
 866 3-5 and (d, h, l, p, t) 4-6 months lead and the initialization dates are shown on the top of each
 867 panel. The GPCP is used for verification. White dashed contours denote ACCs of 0.32,
 868 significant at 95% confidence level by the one-tailed t -test.

869